

Topology detection in cavity QED

Beatriz Pérez-González,¹ Álvaro Gómez-León,² and Gloria Platero¹

¹*Instituto de Ciencia de Materiales de Madrid (ICMM, CSIC)*

²*Instituto de Física Fundamental (IFF, CSIC)*

We explore the physics of topological lattice models in c-QED architectures for arbitrary coupling strength, and the use of the cavity transmission as a topological marker. For this, we develop an approach combining the input-output formalism with Mean-Field theory, which includes self-consistency and quantum fluctuations to first order, and allows to go beyond the small-coupling regime. We apply our formalism to the case of a fermionic Su-Schrieffer-Heeger (SSH) chain coupled to a single-mode cavity. Our findings confirm that the cavity can indeed act as a quantum sensor for topological phases, where the initial state preparation plays a crucial role. Additionally, we discuss the persistence of topological features when the coupling strength increases, in terms of an effective Hamiltonian, and calculate the entanglement entropy. Our approach can be applied to other fermionic systems, opening a route to the characterization of their topological properties in terms of experimental observables.

I. INTRODUCTION

Cavity Quantum Electro-Dynamics (c-QED) studies the interaction between light and matter at the most elementary level, either with individual atoms [1] or solid-state devices, like mesoscopic circuits [2]. Hybrid systems host unique fundamental phenomena due to the appearance of collective light-matter excitations [3], and have revealed themselves as an important tool for the control and manipulation of quantum systems [4]. In particular, they have become an essential landmark in the development of quantum technologies, such as quantum computing [5, 6] or quantum information processing [7]. This is because the coherent interaction of both systems allows for an efficient transfer of information between the two [8, 9], provided that the coupling with the cavity is larger than the losses in the system.

A step further can be taken by considering the combination of quantum light and complex quantum materials with emergent properties, being topological systems an outstanding example [10–13]. Topological phases of matter are characterized by a topological invariant which takes integer values, and whose associated physical properties are robust against a wide number of perturbations. A well-known example are topological insulators (TIs): they have mid-gap states which are exponentially localized at the boundaries and protected by the topological properties of the band structure.

In this work, we investigate the physics of fermionic topological systems placed in c-QED architectures and explore the cavity transmission for arbitrary coupling strength. Our aim is to investigate the use of the cavity transmission as a topological marker, identifying the experimental signatures of non-trivial topological properties, and characterize the physics of the hybrid system. Specifically, we consider the case of a single-mode cavity interacting with a one-dimensional chain described by the SSH model [14–16], a canonical example of TIs, but

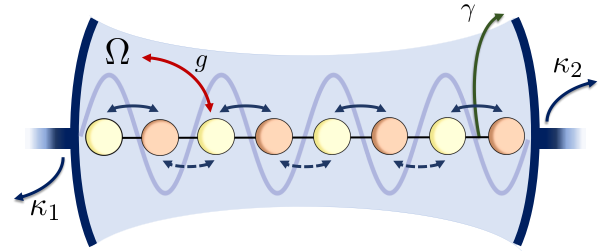


Figure 1: **System Schematic.** Schematic picture of a dimerized chain interacting with the photons in a cavity, of frequency Ω . The cavity is connected to the input and output ports $l = 1, 2$ with factors κ_i ($i = 1, 2$). Fermions and photons interact with coupling strength g , while γ represents the spectral broadening of the fermionic system.

our approach is general and can be applied to other non-trivial topological lattices.

For that purpose, we develop a formalism to calculate t_c for arbitrary coupling in terms of the retarded photonic Green function (GF). We also obtain an analytical expression for the cavity transmission through a generalized input-output formalism, using a mean-field (MF) plus fluctuations analysis, and discuss its validity for different coupling strengths. We find that the transmission can be used to detect non-trivial topology in a fermionic system, with an appropriate state preparation depending on the regime considered. We also derive an effective Hamiltonian to investigate the topological changes produced by the hybridization between photons and fermions, and obtain the entanglement entropy for different partitions of the system.

II. MEAN-FIELD AND FLUCTUATIONS HAMILTONIAN

We consider a mesoscopic system interacting with a cavity, with the following Hamiltonian $H = H_0 + V$, where

$$H_0 = \Omega d^\dagger d + H_S \quad (1)$$

describes the cavity with frequency Ω , being d (d^\dagger) the destruction (creation) photon operator, and H_S corresponds to the single-particle physics of a topological system (which we leave undetermined for the moment). The interaction term V is assumed to have the following form $V = g(d^\dagger + d)Z$, with Z being the fermionic coupling operator. This describes a fermionic system coupled linearly to the cavity field.

We can apply a MF decoupling and write each operator in V as its average plus the fluctuations around it: $\mathcal{O} = \langle \mathcal{O} \rangle + \delta\mathcal{O}$, being $\delta\mathcal{O}$ the fluctuations operator. This results in the following Hamiltonian for the cavity and fermionic system:

$$\begin{aligned} H_0 + V &= H_S + g(\langle d^\dagger \rangle + \langle d \rangle) Z \\ &\quad + \Omega d^\dagger d + g\langle Z \rangle (d^\dagger + d) \\ &\quad + g(\delta d^\dagger + \delta d) \delta Z \end{aligned} \quad (2)$$

The first and the second line in Eq.2 contain the fermionic and photonic MF Hamiltonians, respectively. The third line in Eq.2 contains the term of second order in the fluctuations operators (which we will denote fluctuations Hamiltonian H_δ hereafter), while the scalar contribution has been neglected. Note that the MF Hamiltonians (that contain fluctuation operators only from one of the subsystems) have been rewritten in terms of the original operators using $\delta\mathcal{O} = \mathcal{O} - \langle \mathcal{O} \rangle$. In the asymptotic limits of $g \rightarrow \{0, \infty\}$, fluctuations are completely suppressed and the two systems effectively decouple, making the MF description exact. However, away from these limits, fluctuations are relevant and must be estimated.

Physically, one can see in Eq.2 that if $\langle d \rangle, \langle d^\dagger \rangle \neq 0$, the cavity photons introduce a term proportional to Z in the fermionic Hamiltonian, that can affect the topological properties. Similarly, for $\langle Z \rangle \neq 0$ the photonic part acquires a term analogous to an external field coupled to the photons. Therefore, for a complete characterization one needs to find self-consistent solutions to $\langle Z \rangle$, $\langle d^\dagger \rangle$ and $\langle d \rangle$, which can be easily obtained, to lowest order, from the MF Hamiltonian. To do so, we rotate the photonic MF Hamiltonian $H_\Omega = \Omega d^\dagger d + g(d^\dagger + d)\langle Z \rangle$ with $R = \exp\{-g\langle Z \rangle (d^\dagger - d)/\Omega\}$, to find the following diagonal form:

$$\tilde{H}_\Omega = R^\dagger H_\Omega R = \Omega d^\dagger d - \frac{g^2 \langle Z \rangle^2}{\Omega}. \quad (3)$$

As expected, Eq.3 indicates that, at the MF level, the solely effect of the topological system on the cavity photons is a global shift of all their energies. Importantly, the MF photonic Hamiltonian is diagonal now in the rotated basis, which means that Eq.3 allows to determine the average of the photon operators very easily, resulting in $\langle d^\dagger \rangle + \langle d \rangle = -2g\langle Z \rangle/\Omega$. Now we can write the MF fermionic Hamiltonian in terms of fermionic averages only:

$$\tilde{H}_S = H_S - 2\frac{g^2}{\Omega} \langle Z \rangle Z. \quad (4)$$

This simplifies the calculation of the self-consistency equation for $\langle Z \rangle$, which can now be obtained using an iterative numerical procedure. We make use of Hubbard operators, defined as: $\tilde{X}^{\vec{\alpha}} = \tilde{X}^{\alpha_1, \alpha_2} = |\tilde{\alpha}_1\rangle\langle\tilde{\alpha}_2|$, with $|\tilde{\alpha}_i\rangle$ ($\alpha_i = 1, \dots, N$) being the eigenstates of the MF fermionic Hamiltonian, $\tilde{H}_S|\tilde{\alpha}_i\rangle = \tilde{E}_{\alpha_i}|\tilde{\alpha}_i\rangle$, and $\vec{\alpha} = (\alpha_1, \alpha_2)$. The fluctuations Hamiltonian can also be written in this basis rotating the photonic part with R , to find:

$$\tilde{H}_\delta = R^\dagger H_\delta R = g(d^\dagger + d) \sum_{\vec{\alpha}} \tilde{Z}_{\vec{\alpha}} \tilde{X}^{\vec{\alpha}}, \quad (5)$$

where $\tilde{Z}_{\vec{\alpha}} = \langle \tilde{\alpha}_1 | (Z - \langle Z \rangle) | \tilde{\alpha}_2 \rangle$. Then, \tilde{H}_δ has the same structure as V , though Z has been replaced by the fluctuations operator $\delta Z = Z - \langle Z \rangle$. Indeed, $\tilde{Z}_{\vec{\alpha}}$ measures the effect of fluctuations on the MF eigenstates, and vanishes in the two asymptotic limits, as expected.

III. CALCULATION OF THE CAVITY TRANSMISSION

A. Connection with the photonic Green's function

To account for the measurement of the cavity transmission t_c , we have to include the coupling of the cavity photons to the external modes [17]. By means of input-output theory, we can obtain the input $\tilde{b}_{\text{in},l}$ and output $\tilde{b}_{\text{out},l}$ fields at each of the sides $l = 1, 2$ of the cavity, and write the cavity transmission as the ratio $t_c = \langle \tilde{b}_{\text{out}} \rangle / \langle \tilde{b}_{\text{in}} \rangle$ (see Supplementary Information). Both the phase and the amplitude of $t_c = |t_c|e^{i\varphi}$ are modified by the interaction with the electronic system and can be experimentally measured.

First, we demonstrate a connection between the retarded photonic Green function $G(t, t') = -i\theta(t -$

$t')\langle[d(t), d^\dagger(t')]\rangle$ and t_c . The starting point is the Langevin equation for the cavity field $d(t)$ [5, 17]:

$$\partial_t d(t) = -i\left(\Omega - i\frac{\kappa}{2}\right)d(t) - \sum_{l=1,2} \sqrt{\kappa_l} \tilde{b}_{\text{in},l}(t) - ig \sum_{\bar{\alpha}} \tilde{Z}_{\bar{\alpha}} \tilde{X}^{\bar{\alpha}}(t), \quad (6)$$

where κ_l represents the coupling between the cavity and the outside modes, and $\kappa = \kappa_1 + \kappa_2$. From the reversed-time equation of motion (EoM) one can find the input-output relation $\tilde{b}_{\text{out},l}(t) = \tilde{b}_{\text{in},l}(t) + \sqrt{\kappa_l} d(t)$. Importantly, the notation used for $\tilde{b}_{\text{in},l}(t)$ and $\tilde{b}_{\text{out},l}(t)$ denotes that to the input and output fields are also in the rotated frame (see Supplementary Information).

Now, it is only required to notice that $G(t, t')$, whose EoM yields

$$i\partial_t G(t, t') = \left(\Omega - i\frac{\kappa}{2}\right)G(t, t') + \delta(t - t') - ig\theta(t - t') \sum_{\bar{\alpha}} Z_{\bar{\alpha}} \langle[\tilde{X}^{\bar{\alpha}}(t), d^\dagger(t')]\rangle, \quad (7)$$

is the resolvent of Eq. (6). In Fourier space, this means we can write the photonic operator $d(\omega)$ as (see Supplementary Information)

$$d(\omega) = -iG(\omega) \sum_{l=1,2} \sqrt{\kappa_l} \tilde{b}_{\text{in},l}(\omega). \quad (8)$$

Then, using the previous expression and the input-output relation, one can easily see that

$$t_c(\omega) = \frac{\langle\tilde{b}_{\text{out},2}\rangle}{\langle\tilde{b}_{\text{in},1}\rangle} = -i\sqrt{\kappa_1\kappa_2}G(\omega), \quad (9)$$

where we have assumed the input is only through port 1. This is a key result, since Eq.9 holds for arbitrary values of the coupling constant g . Although an analytical expression for $G(\omega)$ is not possible to achieve for all g , GFs have the advantage that can be exactly obtained using numerical techniques, with the eigenvectors and eigenvalues of the total Hamiltonian.

B. Analytical result for the cavity transmission.

One can see in Eq. 6 that, as the cavity photons couple to the fermionic system, the presence of the term $-ig \sum_{\bar{\alpha}} \tilde{Z}_{\bar{\alpha}} \tilde{X}^{\bar{\alpha}}(t)$ connects the topological properties of the later with the output photons detected at the ports

of the transmission line. The equation of motion for the Hubbard operator yields:

$$\begin{aligned} \partial_t \tilde{X}^{\bar{\alpha}}(t) = & i\left(\tilde{E}_{\bar{\alpha}} - i\frac{\gamma}{2}\right) \tilde{X}^{\bar{\alpha}}(t) \\ & + ig\left(d^\dagger(t) + d(t)\right) \sum_{\beta} \left(\tilde{Z}_{\beta,\alpha_1} \tilde{X}^{\beta,\alpha_2}(t) \right. \\ & \left. - \tilde{Z}_{\alpha_2,\beta} \tilde{X}^{\alpha_1,\beta}(t)\right), \quad (10) \end{aligned}$$

where $\tilde{E}_{\bar{\alpha}} = \tilde{E}_{\alpha_1} - \tilde{E}_{\alpha_2}$, and the phenomenological spectral broadening γ is considered to be equal for all electronic transitions. To close the system of equations and find an analytical solution for $d(\omega)$, a decoupling scheme is required. For this, we notice that contributions from fluctuations are small in the regimes $g \ll \Omega, \tilde{E}_{\bar{\alpha}}$ and $g \gg \Omega, \tilde{E}_{\bar{\alpha}}$ when working in the rotating frame, as discussed in the previous section. Under these conditions, we can rewrite the product $d^{(\dagger)}(t)\tilde{X}^{\bar{\alpha}}(t)$ as

$$d^{(\dagger)}(t)\tilde{X}^{\bar{\alpha}}(t) \approx \langle\tilde{X}^{\bar{\alpha}}\rangle d^{(\dagger)}(t) + \langle d^{(\dagger)}\rangle \tilde{X}^{\bar{\alpha}}(t), \quad (11)$$

Note that we are also neglecting extra correlation terms between photonic and fermionic operators by assuming that fluctuations are small, which would only be relevant near resonances. For the same reason, the expected values $\langle d^{(\dagger)}\rangle$ and $\langle\tilde{X}^{\bar{\alpha}}\rangle$ can then be calculated using the MF Hamiltonians for the cavity and fermionic system, respectively, as shown in the previous section. As a result, the photonic averages *in the rotated frame* can be taken to be $\langle d^{(\dagger)}\rangle \sim 0$. We will also neglect the contribution $\langle\tilde{X}^{\bar{\alpha}}\rangle d^{(\dagger)}(t)$ for being small in the regime of interest [18], although this is not strictly necessary.

With these approximations, we can find a solution for the Hubbard and photonic operators, and together with the input-output relation, write an analytical expression for t_c (see Supplementary Information):

$$t_c = \frac{\langle\tilde{b}_{\text{out},2}\rangle}{\langle\tilde{b}_{\text{in},1}\rangle} = \frac{i\sqrt{\kappa_1\kappa_2}}{\Omega - \omega + g^2\tilde{\chi}(\omega) - i\frac{\kappa}{2}} \quad (12)$$

where $\tilde{\chi}(\omega)$ is the usual electronic susceptibility,

$$\tilde{\chi}(\omega) = \sum_{\bar{\alpha}\beta} \tilde{Z}_{\bar{\alpha}} \frac{\tilde{Z}_{\alpha_2,\beta} \langle\tilde{X}^{\alpha_1,\beta}\rangle - \tilde{Z}_{\beta,\alpha_1} \langle\tilde{X}^{\beta,\alpha_2}\rangle}{\omega + \tilde{E}_{\bar{\alpha}} - i\frac{\gamma}{2}}. \quad (13)$$

It is analogous to the electronic susceptibility for the small- g regime in the standard input-output formalism [18], with the difference that in this case all fermionic parameters are renormalized by the MF self-consistency equations. This allows to extend the validity of Eq. 12

to both the small- g and very-large- g regimes.

As explained before, the statistical averages for the Hubbard operators found in Eq. 13 can be approximated by their MF values: $\langle \tilde{X}^{\bar{\alpha}} \rangle = \delta_{\alpha_1, \alpha_2} p_{\alpha_1}$, being p_{α} the occupation of state $|\bar{\alpha}\rangle$ in the fermionic density matrix $\rho_f = \sum_{\alpha} p_{\alpha} \tilde{X}^{\alpha, \alpha}$. Hence, $\tilde{\chi}(\omega)$ can be written as:

$$\tilde{\chi}(\omega) = \sum_{\bar{\alpha}} \frac{|\tilde{Z}_{\bar{\alpha}}|^2 p_{\bar{\alpha}}}{\omega + \tilde{E}_{\bar{\alpha}} - i\gamma_{\bar{\alpha}}}, \quad (14)$$

with $|\tilde{Z}_{\bar{\alpha}}| = \tilde{Z}_{\alpha_1, \alpha_2} \tilde{Z}_{\alpha_2, \alpha_1}$, and $p_{\bar{\alpha}} = p_{\alpha_1} - p_{\alpha_2}$.

In general, $G(\omega)$ can always be calculated numerically using exact diagonalization. Hence, we can employ Eq.9 to check the accuracy of the analytical result for t_c obtained in Eq.12 (see Supplementary Information). Apart from the small- and very-large- g regimes, in which Eq.12 is specially well-suited, its validity for intermediate coupling strengths can also be tested by comparison with the exact numerical calculation. The results for t_c at arbitrary g are presented in the following section, while further insight into the accuracy of Eq. 12 can be obtained by means of an effective model, which will be also discussed thereupon.

IV. RESULTS

The theoretical framework developed so far is general and can be used for an arbitrary electronic system H_S , with a general coupling operator Z . We apply our formalism to a fermionic 1D topological system described by a tight-binding Hamiltonian with N sites $H_S = \sum_{\langle i, j \rangle=1}^N t_{ij} c_i^{\dagger} c_j$, where t_{ij} is the hopping amplitude and c_i (c_i^{\dagger}) is the destruction (creation) operator for a spinless fermion at site i . Particularizing for the SSH model, a dimerized lattice with alternating hopping pattern, we define the intra- and inter-dimer hopping amplitudes $t = t_0(1 + \delta)$ and $t' = t_0(1 - \delta)$, respectively, with $\delta \in [-1, 1]$. Despite its simplicity, this bipartite structure captures the relevant features of non-trivial topology and gives rise to two distinct topological phases: the trivial phase ($\delta < 0$), which corresponds to the usual two-band insulator, and the topological phase ($\delta > 0$), hosting a pair of topologically protected edge states [14–16]. In the following, we set $t_0 \equiv 1$ as the energy scale for Ω and g .

For the interaction between the cavity and the chain we consider the dipolar approximation, which couples the cavity electric field to the charge density at each site $Z = \sum_i^N x_i c_i^{\dagger} c_i$, being x_i the position in the lattice [19]. Hereafter we consider the origin of positions to be found at the middle of the chain, so that $x_N = -x_1$. If the field wavelength is much larger than the system

dimension, it is a good approximation to assume a constant x_i , to reduce it to a Tavis-Cummings model [20, 21].

A detailed explanation on the solution for $\langle Z \rangle$ can be found in the Supplementary Information. Importantly, our result confirms that in the small- g regime, $\langle Z \rangle = 0$, which implies that the eigenstates of \tilde{H}_S coincide with those of H_S ($\tilde{E}_{\bar{\alpha}} \rightarrow E_{\bar{\alpha}}$, $\tilde{X}^{\bar{\alpha}} \rightarrow X^{\bar{\alpha}}$) and \tilde{H}_{δ} turns into the original V (i.e. $\tilde{Z} \rightarrow Z$). The breakdown of the small- g occurs when $\langle Z \rangle \neq 0$ and the system polarizes.

A. Small- g regime

In the small- g regime, the calculation of the matrix elements $Z_{\bar{\alpha}}$ shows that in a finite system, the cavity can mediate transitions between all eigenstates of the chain, with the exception of the edge states in the topological phase, which exponentially suppress their coupling with the bulk states as a function of the chain length. In consequence, if the system is initially prepared in a bulk state, a measurement of t_c will not reveal the presence of the edge states. The interaction with the electronic system will shift the cavity frequency equally for both the trivial and topological phase, which means that t_c cannot be used as a topological marker in this regime, considering this state preparation.

On the contrary, if the edge state is initially occupied in the topological phase, the transmission peak at $\omega = \Omega$ should remain unaffected by the interaction, as opposed to the behaviour of the trivial phase, in which changes in t_c are expected. This asymmetry between phases can be maximized if the cavity frequency Ω is resonant with an electronic transition $E_{\bar{\alpha}}$ (eigenenergy of the unperturbed fermionic Hamiltonian H_S) and in particular, with the gap of the chain. While the transmission for the non-trivial topological phase does not change compared to the uncoupled cavity transmission (the bulk states are decoupled from the edge states), the presence of a direct resonance in the trivial phase results in a Rabi splitting: the peak of maximum transmission divides into two distinct modes, separated by the Rabi frequency Ω_r [22], which is often detected in experiments and indicates that the regime $g > \{\kappa, \gamma\}$ is achieved [23–27].

This is shown in Fig. 2. We consider the top state in the valence band is occupied for the trivial phase, while the edge state is occupied for the topological phase. This choice is motivated by the fact that both states are adiabatically connected across the topological phase transition, as δ is varied from negative to positive values. While the decoupling between bulk and edge states explains the absence of any changes in t_c for the topological phase, a Rabi splitting appears for the trivial phase. The analytical approximation captures the position of each peak in ω (as indicated by the dashed, grey vertical lines), as

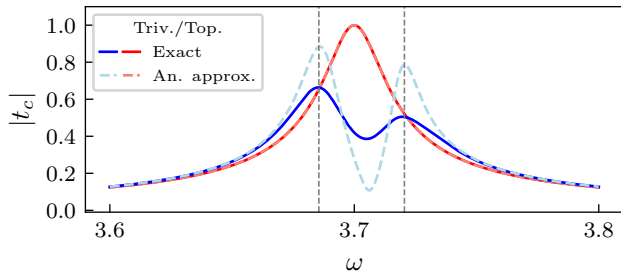


Figure 2: $|t_c(\omega)|$ and $\varphi(\omega)$ as a function of ω . Dashed lines indicate the analytical approximation (Eq. 12), while solid lines correspond to the exact solution (Eq. 9). We consider the $(N/2)$ -th state occupied, corresponding to the edge state in the topological phase and the top of the valence band in the trivial phase. The parameters used are: $\Omega = 3.7$, $g = 0.06$, $\delta = \pm 0.925$ (trivial/topological phase, in blue/red, respectively), $N = 20$, $\gamma = \kappa_1 = \kappa_2 = 0.01$.

well as their relative height, though the exact shape of the peaks is not reproduced. This disagreement can be explained by correlated excitations that strongly modify the system due to resonant conditions.

In conclusion, for the small- g regime it is important to stress that detection of the topological phase requires the system to be initialized in an edge state. Otherwise the cavity transmission cannot differentiate between the two phases.

B. Beyond the small- g regime

We now consider the opposite limit, where $g \gg \Omega, |t_{i,j}|$. The order parameter $\langle Z \rangle \neq 0$, accounting for the backaction between subsystems. In this case the MF eigenstates do not coincide with the unperturbed ones, as the MF correction does not commute with the original Hamiltonian. Now each site has different energy due to the contribution of the term $-2g^2 \langle Z \rangle Z / \Omega$ in \tilde{H}_S (Eq. 4) and the states tend to localize, breaking the original chiral symmetry of the SSH model and destroying the topological order. This is analogous to the Wannier-Stark effect in the presence of a classical DC field. On the other hand, the energy of the cavity photons globally shifts (Eq.3), which means we expect to measure $|t_c| \simeq 1$ again for very large g , because the system is very off-resonant.

All these features are shown in Fig. 3, where we have calculated the transmission at $\omega = \Omega$ for both phases, as a function of the coupling strength g . This includes both the small- g and very-large- g regimes, as well as intermediate coupling strengths. We have chosen $\Omega = 10$, which is far from any resonance with the electronic

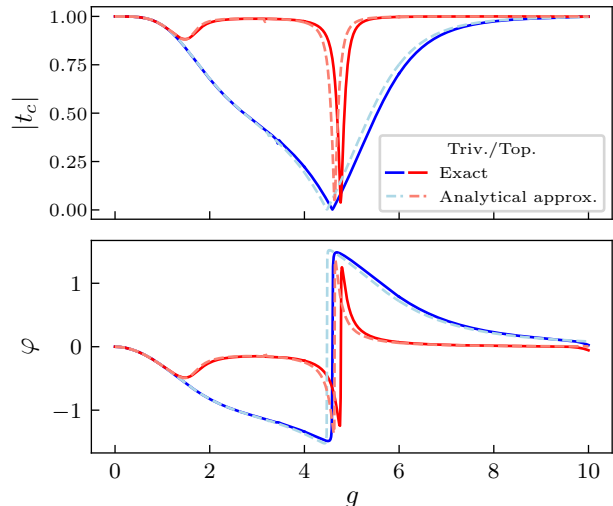


Figure 3: $|t_c(\Omega)|$ and φ as a function of g . Dashed lines indicate the solution from the analytical approximation (Eq. 12), while solid lines correspond to the exact solution (Eq. 9). We consider that the ground state of the chain ($N = 20$) is occupied. The parameters used are: $\omega = \Omega = 10$, $\delta = \pm 0.6$ (trivial/topological phase, in blue/red), $\gamma = \kappa_1 = \kappa_2 = 0.01$.

system. Also, *the calculations are made considering the chain with one particle in its lowest energy state.* For small g , both phases show the same behaviour, as expected: the peak of maximum transmission, initially found at $\omega = \Omega$, shifts due to the interaction. The edge states are transparent to the bulk states and their presence cannot be revealed by measuring t_c with this state preparation. However, Eqs. 12 and 9 predict that the break-down of the small- g regime brings essential differences between the trivial and topological phase, that are enhanced with the interaction: while the trivial phase decays monotonically until reaching a minimum, the topological phase remains mostly unaffected, except for a notorious dip in $|t_c|$ (which corresponds to a change of sign in φ). This is unexpected, as perturbation theory predicts a suppression of the hopping for increasing g and the fast destruction of the topological phase. Thus, the effect of the topological edge states is not washed away by the chiral-symmetry breaking, and the difference between phases can still be detected. Finally, both phases display perfect transmission when g is sufficiently large, in accordance with the MF analysis.

Importantly, the comparison between Eqs. 12 and 9 gives a perfect agreement between the exact numerical result and the analytical approximation for arbitrary g , which means that Eq. 12 captures the behaviour of the system for arbitrary coupling.

V. TOPOLOGICAL FEATURES

A. Effective Hamiltonian

To explore in more detail the different interaction regimes, we derive an effective Hamiltonian using a Schrieffer-Wolff transformation in the basis of eigenstates of the MF Hamiltonian, where the fluctuations Hamiltonian \tilde{H}_δ is considered the perturbation to $\tilde{H}_S + \tilde{H}_\Omega$. We propose the following ansatz for the transformation:

$$S = g(d^\dagger + d) \sum_{\tilde{\alpha}} \frac{\tilde{E}_{\tilde{\alpha}} \tilde{Z}_{\tilde{\alpha}}}{\tilde{E}_{\tilde{\alpha}}^2 - \Omega^2} - g\Omega(d^\dagger - d) \sum_{\tilde{\alpha}} \frac{\tilde{Z}_{\tilde{\alpha}}}{\tilde{E}_{\tilde{\alpha}}^2 - \Omega^2} \tilde{X}_{\tilde{\alpha}} \quad (15)$$

Then, the effective Hamiltonian $\bar{H} = e^S \tilde{H} e^{-S} \simeq \tilde{H}_S + \tilde{H}_\Omega + \frac{1}{2} [S, \tilde{H}_\delta]$ results in the following approximate form (see Supplementary Information):

$$\begin{aligned} \bar{H} \simeq & \sum_{i,j} \tilde{E}_i \tilde{X}^{ii} + \left[\Omega + g^2 \sum_{\tilde{\alpha}} \tilde{\Omega}_{\tilde{\alpha}} \tilde{Y}_{\tilde{\alpha}}^- \right] d^\dagger d \\ & + \frac{g^2}{2} \sum_{\tilde{\alpha}} \tilde{Z}_{\tilde{\alpha}} \sum_{\beta} \left[\frac{\tilde{Z}_{\alpha\beta} \tilde{X}^{\alpha\beta}}{\tilde{E}_{\tilde{\alpha}} - \Omega} - \frac{\tilde{Z}_{\beta\alpha} \tilde{X}^{\beta\alpha}}{\tilde{E}_{\tilde{\alpha}} + \Omega} \right] \quad (16) \end{aligned}$$

with

$$\tilde{\Omega}_{\tilde{\alpha}} = \frac{\tilde{Z}_{\tilde{\alpha}} \tilde{E}_{\tilde{\alpha}}}{\tilde{E}_{\tilde{\alpha}}^2 - \Omega^2}, \quad \tilde{Y}_{\tilde{\alpha}}^- = \sum_{\beta} (\tilde{Z}_{\alpha\beta} \tilde{X}^{\alpha\beta} - \tilde{Z}_{\beta\alpha} \tilde{X}^{\beta\alpha}) \quad (17)$$

To derive Eq.16 we have neglected the small correction provided by two-photon transitions in the rotated frame. The effective Hamiltonian \bar{H} includes a shift in the cavity frequency Ω , proportional to $\tilde{\Omega}_{ij}$ (Eq.17), that depends on the state of the electronic system through $\tilde{Z}_{jn} \langle \tilde{X}^{in} \rangle - \tilde{Z}_{ni} \langle \tilde{X}^{nj} \rangle$, as well as a correction to the MF electronic energies (second line).

Importantly, note that the dependence of the MF electronic Hamiltonian on $\langle Z \rangle$ makes our result non-perturbative, since $\langle Z \rangle$ is a function of the other parameters as well. Indeed, the breakdown of the small- g regime and the consequent polarization of the system with $\langle Z \rangle \neq 0$ triggers the onset of the qualitatively distinct behaviour between both phases shown in t_c shown in Fig. 3). This difference is also captured by \bar{H} : the total frequency shift can be obtained from $\Delta\Omega = g^2 \sum_{ijn} \tilde{\Omega}_{ij} (\tilde{Z}_{jn} \langle \tilde{X}^{in} \rangle - \tilde{Z}_{ni} \langle \tilde{X}^{nj} \rangle)$, where again the expected values are calculated to lowest order using the ground state of \tilde{H}_S . In this case, we can give a simpler expression for the $\Delta\Omega$:

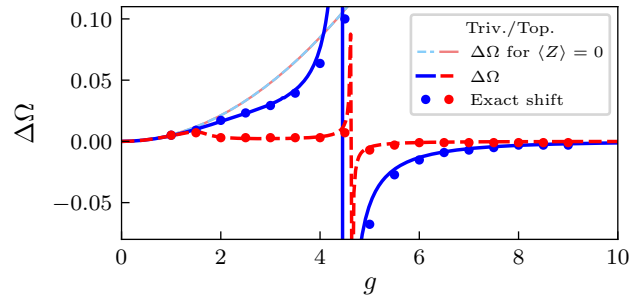


Figure 4: **Cavity shift $\Delta\Omega$ as a function of g .** Plot of the cavity shift $\Delta\Omega$ derived from the effective Hamiltonian (Eq. 18) for both the trivial (blue) and topological (red) phase. The comparison with $\Delta\Omega$ calculated with $\langle Z \rangle$ has been included as well in lighter colors. The dots corresponds to the exact shift obtained from Eq. 9.

$$\Delta\Omega = g^2 \sum_j |\tilde{Z}_{0j}|^2 \frac{\tilde{E}_0 - \tilde{E}_j}{(\tilde{E}_0 - \tilde{E}_j)^2 - \Omega^2}. \quad (18)$$

The cavity shift is plotted in Fig. 4 as a function of g for the same parameters as in Fig. 3. The dots correspond to the exact shift, obtained from the exact numerical t_c (Eq.9), and show an excellent agreement with the predictions from the effective Hamiltonian for arbitrary g . Additionally, $\Delta\Omega$ obtained for $\langle Z \rangle = 0$ ($\tilde{Z} \rightarrow Z$, $\tilde{E}_i \rightarrow E_i$) has been included as well (dashed lines), reinforcing the idea that using t_c as a topological marker is only possible beyond the small- g regime for equilibrium configurations (i.e. ground state occupied): both phases display the same shift when $\langle Z \rangle = 0$. For larger values of g , the divergence in $\delta\Omega$ indicates the presence of a direct resonance between photons and fermions, which should lead to a drop in t_c , in accordance with the minimum in Fig. 3 for both phases. This also confirms that the effective Hamiltonian derived in Eq. 16 is valid for arbitrary g due to the employment of the MF + fluctuations approach. Interestingly, $\Delta\Omega$ changes sign after the divergence. Finally, for $g \sim \Omega$, $\delta\Omega \rightarrow 0$ for both phases, as expected: fluctuations are suppressed and the global shift in the energy of the photons predicted by the MF photonic Hamiltonian (Eq. eq:Photon-rotated) is not detected in t_c .

The change in the eigenenergies of the system due to the interaction is not trivial. First, one has to take into account the polarization of the system and the appearance of the term $2g^2 \langle Z \rangle Z / \Omega$ in the MF Hamiltonian. However, the breaking of the symmetries that provide for topological protection is expected even for small g due to the term in the second line of Eq. 16. Indeed, as g is increased, the topological edge states reduce their energy gradually, and eventually penetrate into the bulk band.

Despite this, they play a crucial role: their presence can still be detected in t_c even after their disappearance into the bulk, thus accounting for the differences in t_c between phases. One can use this correction to the electronic MF eigenstates to measure the effect of fluctuations on the ground state of the MF electronic Hamiltonian (recall that $\tilde{Z}_{ij} = \langle \tilde{i} | (Z - \langle Z \rangle) | \tilde{j} \rangle \equiv \langle \tilde{i} | \delta Z | \tilde{j} \rangle$). A numerical estimation of its magnitude reveals that it is very small, even in the intermediate regime. The fast suppression of fluctuations in the dispersive regime explains why there is such a nice agreement between the exact (Eq. 9) and analytical (Eq. 12) t_c for arbitrary g shown in Fig. 3.

B. Entanglement entropy

Finally, to gain further insight into the topological features of the intermediate coupling regime, we explore the entanglement entropy in the system. The von Neumann entropy is defined as $S_A = -\text{tr}_A \rho_A \ln \rho_A$, where ρ_A corresponds to the reduced density matrix of a subsystem A . When the system is divided in two partitions $A \oplus B$, S_A measures the amount of quantum correlation between them (note that $S_A = S_B$, with S_B defined analogously). The entropy has been used in the study of quantum criticality and topology and has several contributions. In particular, in non-interacting systems one can find boundary contributions related with the Berry phase of the states and with the presence of edge modes [28].

In our case, we can partition the system in two different ways. First, we consider a partition separating the fermionic chain and the cavity, and calculate S_{fer} by tracing out the photonic degrees of freedom (Fig. 5(a)). In that case, we can see that S_{el} grows with g and suddenly drops at a critical coupling strength value, which is different for the trivial and topological phase and reproduces the phase transition captured by the order parameter $\langle Z \rangle$ (see Supplementary Information). However, the differences between both phases at finite coupling are not clarified for this partition.

The alternative partition requires to first integrate out the photonic degrees of freedom. The resulting density matrix for the fermionic chain encodes the role of photons and can be divided in two parts $A = \{1, 2, \dots, N_A\}$ and $B = \{N_A + 1, N_A + 2, \dots, N\}$ (with $N_A \neq N/2$) of which the entropy can be calculated. This is interesting from a topological perspective, because the entanglement between these partitions has been already studied in non-interacting SSH chains and can differentiate between the trivial and the topological phase [28]. In our case the fermionic reduced density matrix is dressed by photons, which makes the model more interesting from a fundamental perspective, as we are dealing with many-body topological models.

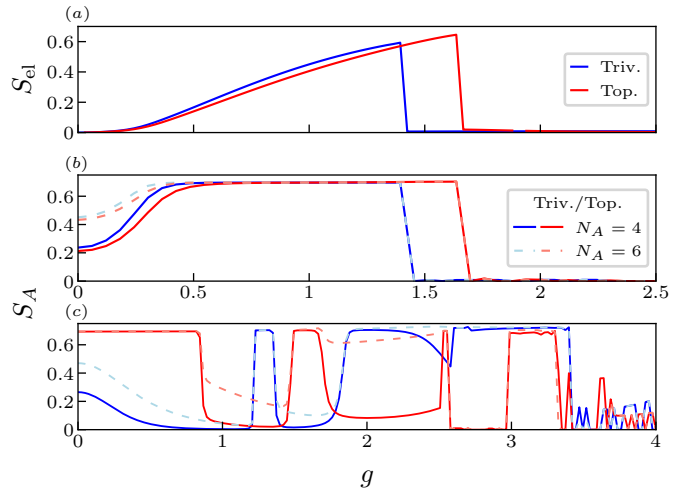


Figure 5: **Entanglement entropy for different partitions.** (a) S_{el} ($N = 20$) for the ground state, with $\Omega = 10$, $|\delta| = 0.6$, and $N = 20$. It grows as the coupling is increased, dropping to zero when the fermionic system polarizes. (b) S_A as a function of g for different partitions N_A and the system in its ground state. As in the previous case, S_A increases with the coupling until it drops to zero. (c) S_A for the system in its $N/2$ -th state, analogous to half-filling in the non-interacting case. The topological phase initially displays a quantized value $S_A = \log 2$ independent of the partition, indicating the presence of an edge state.

In Fig. 5(b) we plot the entanglement entropy for the system in its ground state. In general, the entropy increases as a function of g for both phases and saturates to $\log 2$, dropping to zero as the expectation value $\langle Z \rangle$ acquires a finite value. In that sense its behavior is similar to that of Fig. 5(a) and can be used to obtain information about the phase diagram for the order parameter. Interestingly, the saturation to $\log 2$ indicates that the ground state becomes a cat state for finite g , which is destroyed when the system polarizes (i.e., $\langle Z \rangle \neq 0$), turning into a fully localized state. However, it does not provide new insight into the topological characterization of the system, as it only differentiates between the two phases in the range of values comprised between their respective critical g .

In contrast, Fig. 5(c) considers the $N/2$ -th state occupied (this is specially relevant to compare with half-filling in a non-interacting SSH chain). This state coincides with the edge state in the topological phase and with the top of the valence band in the trivial phase for the isolated chain. In this case the topological phase displays a quantized value $S_A = \log 2$ for small g , independent of the partition, while for the trivial phase S_A is smaller and changes for different partitions N_A . The $\log 2$ value is a consequence of a maximally entangled cat state and its independence on the partition indicates that it is lo-

calized at the boundaries of the system (i.e., the bulk does not contribute and all entropy comes from the entanglement between the two edges [28]). Then, we can see that the topological boundary mode is present until the entropy drops, indicating the destruction of entanglement for the $N/2$ -th state. This coincides with the first anti-crossing of the edge state with a bulk state as they penetrate in the bulk bands (see Supplementary Information).

The persistence of the $\log(2)$ value for S_A in the topological chain for small g means the interaction preserves the entanglement between ending sites created by the original topological boundary modes, though their energy and localization length does change due to the symmetry-breaking terms in the effective Hamiltonian. This can have important implications for designing quantum information protocols with c-QED structures in which correlation between distant sites of the fermionic system needs to be exploited, which in this case is naturally provided by the topological features of the chain. Importantly, the topological contribution to the entanglement does not disappear after S_A drops to zero at $g \sim 0.8$, but migrates from one state to the other as the anti-crossing originated by the edge states entering the band take place in the energy spectrum (see Supplementary Information).

Interestingly, increasing g leads to a succession of new $\log 2$ plateaus, indicating that boundary modes are linked with both the original trivial and the topological phases [29–31]. Again, each abrupt change in S_A coincides with an anti-crossing between the $N/2$ -th and other states in the upper bands (see Supplementary Information). Finally, when g approaches the divergence in Fig. 4 the entropy drops for both phases and the presence of boundary modes is completely washed out by the interaction with the cavity.

The existence of edge states in the energy spectrum in both phases for large g is a consequence of the form of the fermionic coupling operator Z , which acts more strongly at the ending sites of the chain than in the middle region. It is very enlightening to compare these results with the ones obtained by setting $x_i \equiv x$ (which would be the case if the size of the fermionic system was negligible in comparison with the wavelength of the electric field in the cavity). Such a interaction model would not create any entanglement neither between photons and fermions, nor within the ending sites of the fermionic chain, and would not give rise to these $\log(2)$ plateaus.

VI. CONCLUSIONS

In this work, we have investigated the use of the cavity transmission t_c as a topological marker for arbitrary coupling regimes in an hybrid system, composed of

a quantum cavity coupled to a fermionic lattice with distinct topological phases. Both the amplitude $|t_c|$ and phase φ can be experimentally measured, carrying information about the fermionic system interacting with the cavity. For this purpose, we have developed a framework combining two perspectives: first, we have employed the retarded photonic Green function to obtain an exact result for t_c for arbitrary coupling strengths; second, we have combined input-output formalism with a MF plus fluctuations analysis to derive an analytical expression whose validity can be extended beyond the small- g regime. Exploring how the interaction affects the topological properties of the fermionic system is also the aim of this work.

To illustrate our results we have considered a topological SSH chain interacting via the dipolar coupling with the cavity. We reproduce the expected results for small g , where it is well-known that the transmission allows for dispersive readout of the properties of the fermionic system. Detecting differences between phases with distinct topology is possible if the system is initialized in its edge state, due to their transparency to the bulk states: while the cavity can mediate many transitions between the bulk states, the edge states remain isolated from them. One disadvantage of this regime of operation is that the measurement needs to be carried out before thermalization happens, but this could be avoided by filling the fermionic system to half-filling (however, in this case many systems require to account for particle interactions as well).

Beyond the small- g regime, differences between topological phases are enhanced, and importantly, they can be detected for the ground state, indicating that the measurement can be performed when the system has thermalized. This means that the presence of the edge states still has an impact on the cavity transmission, despite the chiral symmetry breaking induced by the coupling. To study this regime in more depth, we have derived an effective Hamiltonian encoding the role of fluctuations to first order.

Finally, we have also studied the entanglement entropy between different partitions of the total system (Fig. 5), and how this quantity connects with the previous results. As expected, we verify the entanglement between photons and fermions increases as the coupling strength gets larger, which is crucial for many applications of c-QED architectures [32, 33], up to a critical value at which it suddenly drops to zero. We also explored the entanglement between two asymmetric partitions of the SSH chain, once the photonic degrees of freedom have been traced out. This sheds light on how the interaction affects the eigenstates of the chain, and how the entanglement created by the edge states is maintained for large values of the coupling, even after

they have penetrated into the bulk bands.

Regarding the experimental implementations, crucial milestones have been achieved on different platforms that pave the way for the realization of the findings discussed in this work.

On one hand, quantum dots (QDs) offer a scalable, highly-tunable solid state platform, in which the control and manipulation of long arrays has already been reached [34–36], including the simulation of fundamental models [37, 38]. When placed inside cavities, different experiments have proven to fulfill the condition $g > \{\kappa, \gamma\}$, both in double [24–27, 39–46] and triple QDs [23, 47].

Another suitable option for implementation could be cold atoms, where the simulation of complex Hamiltonians with non-trivial topological properties has already been studied [48] and implemented [49]. They offer great versatility and control in c-QED experiments [50]: atoms can be loaded deterministically inside the cavity, which allows to tailor the atom-field coupling on demand [51, 52], as well as long coherence times [51, 53]. The condition $g > \{\kappa, \gamma\}$ has also been achieved [51, 53–61]. Regarding the model Hamiltonian, it is only required to notice that the hopping term can be written as $\sum_{i,j} t_{i,j} \sigma_i^+ \sigma_j^-$ and the fermionic part of the interaction can be mapped to a Zeeman term that changes linearly with the position $\sum_i B_i^z \sigma_i^z$. This can also be extrapolated to trapped ions [62].

With the previous figures of merit in mind, the current state-of-the-art techniques for these platforms would allow to implement the topological detection method discussed for the small- g regime, in which t_c can be used as a topological marker if the edge state is occupied (see Fig. 2). However, larger coupling strengths have already been realized with superconducting qubits [63]. The condition $g > \{\gamma, \kappa\}$ is very well-established [64], but more significant is the achievement of further regimes of interaction in which the coupling to the resonator can reach values comparable to the energy of the qubit [65–68]. Additionally, the SSH model considered in this work has also been realized using superconducting

qubits [69]. Therefore, this would be a feasible platform to implement the topology detection discussed for arbitrary coupling strengths with the current techniques.

As an outlook, we believe our work provides a solid basis to study topological systems coupled to quantum cavities, while opening the way to complementary research. For example, including the role of electron interactions using a Hubbard term, or developing an effective Hamiltonian to study the resonant case in more depth. Besides, other interaction models for the cavity and fermionic system could be addressed in order to connect with experiments performed on different set-ups, such as having only one of the sites of the fermionic chain connected to the cavity. This would be the case of the already experimental implementation of QD chains coupled to cavities mentioned in the former section. Lastly, the employment of the entanglement entropy to study the effect of the interaction upon the fermionic system sets a precedent in the field, since it is usually used to characterize topology in non-interacting systems.

Acknowledgements

We thank M. Benito and S. Kohler for fruitful discussions.

This work was supported by: Ministerio de Economía y Competitividad, through Grant MAT2017- 86717-P (CSIC Research Platform PTI-001) and PID2020-117787GB-I00, Ministerio de Educación y Formación Profesional, under the program FPU, with reference FPU17/05297 (B. P.-G.), the Spanish project PGC2018-094792-B-100 (MCIU/AEI/FEDER, EU) (A. G.-L.). B.P.G. did the analytical and numerical analysis under the supervision of A.G.L. and G.P. All authors discussed and analyzed the results and all authors wrote the paper. The authors declare that they do not have any competing interests.

-
- [1] H. Walther, B. T. H. Varcoe, B.-G. Englert, and T. Becker, Reports on Progress in Physics **69**, 1325 (2006), URL <https://doi.org/10.1088%2F0034-4885%2F69%2F5%2F02>.
 - [2] A. Cottet, M. C. Dartiailh, M. M. Desjardins, T. Cubaynes, L. C. Contamin, M. Delbecq, J. J. Viennot, B. Doucot, and T. Kontos, J. Phys.: Condens. Matter **29** (2017).
 - [3] R. H. Dicke, Phys. Rev. **93**, 99 (1954), URL <https://link.aps.org/doi/10.1103/PhysRev.93.99>.
 - [4] J. Li and M. Eckstein, Phys. Rev. Lett. **125**, 217402 (2020), URL <https://link.aps.org/doi/10.1103/PhysRevLett.125.217402>.
 - [5] A. Blais, R.-S. Huang, A. Wallraff, S. M. Girvin, and R. J. Schoelkopf, Phys. Rev. A **69**, 062320 (2004), URL <https://link.aps.org/doi/10.1103/PhysRevA.69.062320>.
 - [6] T. Pellizzari, S. A. Gardiner, J. I. Cirac, and P. Zoller, Phys. Rev. Lett. **75**, 3788 (1995).
 - [7] A. Blais, J. Gambetta, A. Wallraff, D. I. Schuster, S. M. Girvin, M. H. Devoret, and R. J. Schoelkopf, Phys. Rev. A **75**, 032329 (2007).
 - [8] D. Matsukevich and A. Kuzmich, Science **306**, 663 (2004).
 - [9] J. I. Cirac, P. Zoller, H. J. Kimble, and H. Mabuchi, Phys. Rev. Lett. **78**, 3221 (1997), URL <https://link.aps.org/doi/10.1103/PhysRevLett.78.3221>.

- aps.org/doi/10.1103/PhysRevLett.78.3221.
- [10] C. A. Downing, T. J. Sturges, G. Weick, M. Stobińska, and L. Martín-Moreno, *Phys. Rev. Lett.* **123**, 217401 (2019), URL <https://link.aps.org/doi/10.1103/PhysRevLett.123.217401>.
 - [11] W. Nie and Y.-x. Liu, *Phys. Rev. Research* **2**, 012076 (2020), URL <https://link.aps.org/doi/10.1103/PhysRevResearch.2.012076>.
 - [12] M. C. Dartiailh, T. Kontos, B. Douçot, and A. Cottet, *Phys. Rev. Lett.* **118**, 126803 (2017), URL <https://link.aps.org/doi/10.1103/PhysRevLett.118.126803>.
 - [13] O. Dmytruk, M. Trif, and P. Simon, *Phys. Rev. B* **92**, 245432 (2015).
 - [14] B. Pérez-González, M. Bello, A. Gómez-León, and G. Platero, *Phys. Rev. B* **99**, 035146 (2019), URL <https://link.aps.org/doi/10.1103/PhysRevB.99.035146>.
 - [15] B. Pérez-González, M. Bello, G. Platero, and A. Gómez-León, *Phys. Rev. Lett.* **123**, 126401 (2019).
 - [16] M. Bello, C. Creffield, and G. Platero, *Scientific Reports* **6** (2016).
 - [17] C. Gardiner and P. Zoller, *Quantum Noise: A Handbook of Markovian and Non-Markovian Quantum Stochastic Methods with Applications to Quantum Optics* (Springer-Verlag Berlin Heidelberg, 2004).
 - [18] S. Kohler, *Phys. Rev. A* **98**, 023849 (2018), URL <https://link.aps.org/doi/10.1103/PhysRevA.98.023849>.
 - [19] A. Cottet, T. Kontos, and B. Douçot, *Phys. Rev. B* **91**, 205417 (2015), URL <https://link.aps.org/doi/10.1103/PhysRevB.91.205417>.
 - [20] M. Tavis and F. W. Cummings, *Phys. Rev.* **170**, 379 (1968), URL <https://link.aps.org/doi/10.1103/PhysRev.170.379>.
 - [21] M. TAVIS and F. W. CUMMINGS, *Phys. Rev.* **188**, 692 (1969), URL <https://link.aps.org/doi/10.1103/PhysRev.188.692>.
 - [22] D. F. Walls and G. J. Milburn, *Quantum Optics* (Springer, 2008).
 - [23] A. J. Landig, J. V. Koski, P. Scarlino, U. C. Mendes, A. Blais, C. Reichl, W. Wegscheider, A. Wallraff, K. Ensslin, and T. Ihn, *Nature* **560**, 179 (2018).
 - [24] A. Stockklauser, P. Scarlino, J. V. Koski, S. Gasparinetti, C. K. Andersen, C. Reichl, W. Wegscheider, T. Ihn, K. Ensslin, and A. Wallraff, *Phys. Rev. X* **7**, 011030 (2017), URL <https://link.aps.org/doi/10.1103/PhysRevX.7.011030>.
 - [25] X. Mi, M. Benito, S. Putz, D. M. Zajac, J. M. Taylor, G. Burkard, and J. R. Petta, *Nature* **555**, 590 (2018).
 - [26] N. Samkharadze, G. Zheng, N. Kalhor, D. Brousse, A. Sammak, U. C. Mendes, A. Blais, G. Scappucci, and L. M. K. Vandersypen, *Science* **359**, 1123 (2018).
 - [27] X. Mi, J. M. Cady, D. M. Zajac, P. W. Deelman, and J. R. Petta, *Science* **355** (2017).
 - [28] S. Ryu and Y. Hatsugai, *Phys. Rev. B* **73**, 245115 (2006), URL <https://link.aps.org/doi/10.1103/PhysRevB.73.245115>.
 - [29] V. Gurarie, *Phys. Rev. B* **83**, 085426 (2011), URL <https://link.aps.org/doi/10.1103/PhysRevB.83.085426>.
 - [30] S. R. Manmana, A. M. Essin, R. M. Noack, and V. Gurarie, *Phys. Rev. B* **86**, 205119 (2012), URL <https://link.aps.org/doi/10.1103/PhysRevB.86.205119>.
 - [31] A. Gómez-León, *Phys. Rev. B* **94**, 035144 (2016), URL <https://link.aps.org/doi/10.1103/PhysRevB.94.035144>.
 - [32] H. Kimble, *Nature* **453**, 1023 (2008).
 - [33] J. M. Raimond, M. Brune, and S. Haroche, *Rev. Mod. Phys.* **73**, 565 (2001), URL <https://link.aps.org/doi/10.1103/RevModPhys.73.565>.
 - [34] D. M. Zajac, T. M. Hazard, X. Mi, E. Nielsen, and J. R. Petta, *Phys. Rev. Applied* **6**, 054013 (2016), URL <https://link.aps.org/doi/10.1103/PhysRevApplied.6.054013>.
 - [35] C. Volk, A. M. J. Zwerver, U. Mukhopadhyay, P. T. Eendebak, C. J. van Diepen, J. P. Dehollain, T. Hensgens, T. Fujita, C. Reichl, W. Wegscheider, et al., *npj Quantum Information* **5** (2019).
 - [36] W. I. L. Lawrie, H. G. J. Eenink, N. W. Hendrickx, J. M. Boter, L. Petit, S. V. Amitonov, M. Lodari, B. Paquette Wuetz, C. Volk, S. G. J. Philips, et al., *Applied Physics Letters* **116**, 080501 (2020).
 - [37] T. Hensgens, T. Fujita, L. Janssen, X. Li, C. J. Van Diepen, C. Reichl, W. Wegscheider, S. Das Sarma, and L. M. K. Vandersypen, *Nature* **548**, 70 (2017).
 - [38] J. P. Dehollain, U. Mukhopadhyay, V. P. Michal, Y. Wang, B. Wunsch, C. Reichl, W. Wegscheider, M. S. Rudner, E. Demler, and L. M. K. Vandersypen, *Nature* **579**, 528 (2020), ISSN 1476-4687, URL <https://doi.org/10.1038/s41586-020-2051-0>.
 - [39] A. Stockklauser, P. Scarlino, J. V. Koski, S. Gasparinetti, C. K. Andersen, C. Reichl, W. Wegscheider, T. Ihn, K. Ensslin, and A. Wallraff, *Phys. Rev. X* **7**, 011030 (2017), URL <https://link.aps.org/doi/10.1103/PhysRevX.7.011030>.
 - [40] L. E. Bruhat, T. Cubaynes, J. J. Viennot, M. C. Dartiailh, M. M. Desjardins, A. Cottet, and T. Kontos, *Phys. Rev. B* **98**, 155313 (2018), URL <https://link.aps.org/doi/10.1103/PhysRevB.98.155313>.
 - [41] D. J. van Woerkom, P. Scarlino, J. H. Ungerer, C. Müller, J. V. Koski, A. J. Landig, C. Reichl, W. Wegscheider, T. Ihn, K. Ensslin, et al., *Phys. Rev. X* **8**, 041018 (2018), URL <https://link.aps.org/doi/10.1103/PhysRevX.8.041018>.
 - [42] B. Wang, T. Lin, H. Li, S. Gu, M. Chen, G. Guo, H. Jiang, X. Hu, G. Cao, and G. Guo, *Science Bulletin* **66**, 332 (2021), ISSN 2095-9273, URL <https://www.sciencedirect.com/science/article/pii/S2095927320306587>.
 - [43] D. Najer, I. Söller, P. Sekatski, V. Dolique, M. C. Löbl, D. Riedel, R. Schott, S. Starosielec, S. R. Valentin, A. Wieck, et al., *Nature* **5**, 622 (2019).
 - [44] N. Samkharadze, G. Zheng, N. Kalhor, D. Brousse, A. Sammak, U. C. Mendes, A. Blais, G. Scappucci, and L. M. K. Vandersypen, *Science* **359** (2018).
 - [45] T. Cubaynes, M. R. Delbecq, M. C. Dartiailh, R. Assouly, M. M. Desjardins, L. C. Contamin, L. E. Bruhat, Z. Leghtas, F. Mallet, A. Cottet, et al., *npj Quantum Information* **5** (2019).
 - [46] X. G. Borjans, F. Croot, X. Mi, M. J. Gullans, and J. R. Petta, *Nature* **577**, 195 (2020).
 - [47] A. J. Landig, J. V. Koski, P. Scarlino, C. Müller, J. C. Abadillo-Uriel, B. Kratochwil, C. Reichl, W. Wegscheider, S. N. Coppersmith, M. Friesen, et al., *Nature Communications* **10** (2019).
 - [48] D.-W. Zhang, Y.-Q. Zhu, Y. X. Zhao, H. Yan, and S.-L. Zhu, *Advances in Physics* **67**, 253 (2018).
 - [49] M. Atala, M. Aidelsburger, J. T. Barreiro, D. Abanin, T. Kitagawa, E. Demler, and I. Bloch, *Nature Physics* **9**, 795 (2013).
 - [50] H. Ritsch, P. Domokos, F. Brennecke, and T. Esslinger,

- Rev. Mod. Phys. **85**, 553 (2013), URL <https://link.aps.org/doi/10.1103/RevModPhys.85.553>.
- [51] K. M. Fortier, S. Y. Kim, M. J. Gibbons, P. Ahmadi, and M. S. Chapman, Phys. Rev. Lett. **98**, 233601 (2007), URL <https://link.aps.org/doi/10.1103/PhysRevLett.98.233601>.
- [52] S. Nußmann, M. Hijkema, B. Weber, F. Rohde, G. Rempe, and A. Kuhn, Phys. Rev. Lett. **95**, 173602 (2005), URL <https://link.aps.org/doi/10.1103/PhysRevLett.95.173602>.
- [53] S. Nußmann, K. Murr, M. Hijkema, B. Weber, A. Kuhn, and G. Rempe, Nature Physics **1**, 122 (2005).
- [54] A. D. Boozer, A. Boca, R. Miller, T. E. Northup, and H. J. Kimble, Phys. Rev. Lett. **97**, 083602 (2006), URL <https://link.aps.org/doi/10.1103/PhysRevLett.97.083602>.
- [55] A. Boca, R. Miller, K. M. Birnbaum, A. D. Boozer, J. McKeever, and H. J. Kimble, Phys. Rev. Lett. **93**, 233603 (2004), URL <https://link.aps.org/doi/10.1103/PhysRevLett.93.233603>.
- [56] P. Maunz, T. Puppe, I. Schuster, N. Syassen, P. Pinkse, and G. Rempe, Nature **428**, 50 (2004).
- [57] J. McKeever, A. Boca, A. D. Boozer, R. Miller, J. R. Buck, A. Kuzmich, and H. J. Kimble, Science **303**, 1992 (2004), ISSN 0036-8075, <https://science.sciencemag.org/content/303/5666/1992.full.pdf>, URL <https://science.sciencemag.org/content/303/5666/1992>.
- [58] J. Ye, D. W. Vernooy, and H. J. Kimble, Phys. Rev. Lett. **83**, 4987 (1999), URL <https://link.aps.org/doi/10.1103/PhysRevLett.83.4987>.
- [59] J. McKeever, J. R. Buck, A. D. Boozer, and H. J. Kimble, Phys. Rev. Lett. **93**, 143601 (2004), URL <https://link.aps.org/doi/10.1103/PhysRevLett.93.143601>.
- [60] J. A. Sauer, K. M. Fortier, M. S. Chang, C. D. Hamley, and M. S. Chapman, Phys. Rev. A **69**, 051804 (2004), URL <https://link.aps.org/doi/10.1103/PhysRevA.69.051804>.
- [61] J. McKeever, J. R. Buck, A. D. Boozer, A. Kuzmich, H.-C. Nägerl, D. M. Stamper-Kurn, and H. J. Kimble, Phys. Rev. Lett. **90**, 133602 (2003), URL <https://link.aps.org/doi/10.1103/PhysRevLett.90.133602>.
- [62] V. Bužek, G. Drobný, M. S. Kim, G. Adam, and P. L. Knight, Phys. Rev. A **56**, 2352 (1997), URL <https://link.aps.org/doi/10.1103/PhysRevA.56.2352>.
- [63] X. Gu, A. F. Kockum, A. Miranowicz, Y. xi Liu, and F. Nori, Physics Reports **718-719**, 1 (2017), ISSN 0370-1573, microwave photonics with superconducting quantum circuits, URL <https://www.sciencedirect.com/science/article/pii/S0370157317303290>.
- [64] D. I. Schuster, A. A. Houck, J. A. Schreier, A. Wallraff, J. M. Gambetta, A. Blais, L. Frunzio, J. Majer, B. Johnson, M. H. Devoret, et al., Nature **445**, 515 (2007), ISSN 1476-4687, URL <https://doi.org/10.1038/nature05461>.
- [65] A. Baust, E. Hoffmann, M. Haeberlein, M. J. Schwarz, P. Eder, J. Goetz, F. Wulschner, E. Xie, L. Zhong, F. Quijandria, et al., Phys. Rev. B **93**, 214501 (2016), URL <https://link.aps.org/doi/10.1103/PhysRevB.93.214501>.
- [66] P. Forn-Díaz, J. Lisenfeld, D. Marcos, J. J. García-Ripoll, E. Solano, C. J. P. M. Harmans, and J. E. Mooij, Phys. Rev. Lett. **105**, 237001 (2010), URL <https://link.aps.org/doi/10.1103/PhysRevLett.105.237001>.
- [67] T. Niemczyk, F. Deppe, H. Huebl, E. P. Menzel, F. Hocke, M. J. Schwarz, J. J. Garcia-Ripoll, D. Zueco, T. Hümmer, E. Solano, et al., Nature Physics **6**, 772 (2010), ISSN 1745-2481, URL <https://doi.org/10.1038/nphys1730>.
- [68] F. Yoshihara, T. Fuse, S. Ashhab, K. Kakuyanagi, S. Saito, and K. Semba, Nature Physics **13**, 44 (2017), ISSN 1745-2481, URL <https://doi.org/10.1038/nphys3906>.
- [69] I. S. Besedin, M. A. Gorlach, N. N. Abramov, I. Tsitsilin, I. N. Moskalenko, A. A. Dobronosova, D. O. Moskalev, A. R. Matanin, N. S. Smirnov, I. A. Rodionov, et al., Phys. Rev. B **103**, 224520 (2021), URL <https://link.aps.org/doi/10.1103/PhysRevB.103.224520>.

SUPPLEMENTARY INFORMATION

Appendix A: Input-output formalism

Using the initial Hamiltonian

Consider the initial Hamiltonian describing a transmission line with two ports, coupled to the topological system via the cavity photons. The total Hamiltonian is:

$$H = \Omega d^\dagger d + H_S + g(d^\dagger + d)Z + H_B, \quad (\text{A1})$$

with H_B being the Hamiltonian for the electromagnetic field in the transmission line and its coupling to the cavity,

$$H_B = \sum_{l=1,2} \int_{-\infty}^{\infty} \omega b_l^\dagger(\omega) b_l(\omega) d\omega + i \sum_{l=1,2} \int_{-\infty}^{\infty} \left[\mu_l(\omega) b_l^\dagger(\omega) d - \mu_l(\omega)^* d^\dagger b_l(\omega) \right] d\omega \quad (\text{A2})$$

where $l = 1, 2$ represent the left/right sides of the cavity, $b_l(\omega)$ is the destruction operator for a photon with energy ω at side l of the cavity and $\mu_l(\omega)$ represents the coupling between the cavity and the outside modes. In this work, we will consider the Markov approximation, which gives $\mu_l(\omega) = \sqrt{\kappa_l/2\pi}$.

Then, the first step is to derive the equation of motion (EoM) for the transmission line photons:

$$\frac{d}{dt} b_l(\nu, t) = -i\nu b_l(\nu, t) + \sqrt{\frac{\kappa_l}{2\pi}} d(t) \quad (\text{A3})$$

which can be formally integrated to yield

$$b_l(\nu, t) = b_l(\nu, t_0) e^{-i\nu(t-t_0)} + \sqrt{\frac{\kappa_l}{2\pi}} \int_{t_0}^t dt' e^{-i\nu(t-t')} d(t') \quad (\text{A4})$$

where $t_0 < t$ represents the initial condition. Inserting the previous expression into the EoM for the cavity photons, we get

$$\begin{aligned} \frac{d}{dt} d(t) &= -i\Omega d(t) - igZ(t) - \sum_{l=1,2} \sqrt{\frac{\kappa_l}{2\pi}} \int_{-\infty}^{\infty} d\nu b_l(\nu, t) \\ &= -i \left(\Omega - i\frac{\kappa}{2} \right) d(t) - igZ(t) \\ &\quad - \sum_{l=1,2} \sqrt{\kappa_l} b_{in,l}(t) \end{aligned} \quad (\text{A5})$$

where $\kappa = \kappa_1 + \kappa_2$, and we have defined an input field,

$$b_{in,l}(t) = \frac{1}{\sqrt{2\pi}} \int_{-\infty}^{\infty} b_l(\nu, t_0) e^{-i\nu(t-t_0)} d\nu. \quad (\text{A6})$$

Similarly, the solution for $b_l(\nu, t)$ in (A4) can also be obtained in terms of a final condition $t_1 > t$, which let us define an output field $b_{out,l}(t)$, fulfilling

$$b_{out,l}(t) = b_{in,l}(t) + \sqrt{\kappa_l} d(t) \quad (\text{A7})$$

One has to solve the EoM for $Z(t)$ as well. We consider the basis of eigenstates of the fermionic Hamiltonian

$$H_S = \sum_{\alpha=1}^N E_{\alpha} X^{\alpha,\alpha}, \quad Z = \sum_{\bar{\alpha}} Z_{\bar{\alpha}} X^{\bar{\alpha}} \quad (\text{A8})$$

with $X^{\bar{\alpha}} = X^{\alpha_1, \alpha_2} = |\alpha_1\rangle\langle\alpha_2|$, and calculate the equation of motion for an arbitrary Hubbard operator $X^{\bar{\alpha}}$

$$\begin{aligned} \partial_t \tilde{X}^{\bar{\alpha}}(t) &= i \left(\tilde{E}_{\bar{\alpha}} - i\frac{\gamma}{2} \right) \tilde{X}^{\bar{\alpha}}(t) \\ &\quad + ig \left(d^{\dagger}(t) + d(t) \right) \sum_{\beta} \left(\tilde{Z}_{\beta, \alpha_1} \tilde{X}^{\beta, \alpha_2}(t) \right. \\ &\quad \left. - \tilde{Z}_{\alpha_2, \beta} \tilde{X}^{\alpha_1, \beta}(t) \right), \end{aligned} \quad (\text{A9})$$

where $E_{\bar{\alpha}} = E_{\alpha_1} - E_{\alpha_2}$ and we have also included the phenomenological spectral broadening factor $\gamma/2$. The product $d^{(\dagger)}(t) X(t)$ can be decomposed as

$$d^{(\dagger)}(t) X(t) \approx \langle X \rangle d^{(\dagger)}(t) + \langle d^{(\dagger)} \rangle X(t), \quad (\text{A10})$$

where we are neglecting any terms accounting for correlation between operators, which is true in the small- g regime. Under this condition, one can safely calculate $\langle X \rangle$ and $\langle d^{(\dagger)} \rangle$ using the corresponding unperturbed Hamiltonians, H_S and $\Omega d^{\dagger} d$, respectively. Then, one can easily see that $\langle d^{(\dagger)} \rangle = 0$, and hence the solution for the EoM in (A9) in frequency space reads

$$X^{\bar{\alpha}}(\omega) \simeq g d(\omega) \frac{\sum_{\beta} (Z_{\alpha_2, \beta} \langle X^{\alpha_1, \beta} \rangle - Z_{\beta, \alpha_1} \langle X^{\beta, \alpha_2} \rangle)}{\omega + E_{\bar{\alpha}} - i\frac{\gamma}{2}}. \quad (\text{A11})$$

We have also neglected the contribution of $\langle X \rangle d^{\dagger}(\omega)$, as typically done in the literature [18]. Substituting this result in (A5), we find

$$d(\omega) = \frac{i \sum_{l=1,2} \sqrt{\kappa_l} b_{in,l}(\omega)}{\Omega - \omega - i\frac{\kappa}{2} + g^2 \chi(\omega)} \quad (\text{A12})$$

where

$$\chi(\omega) = \sum_{\bar{\alpha}, \beta} \frac{Z_{\bar{\alpha}} (Z_{\alpha_2, \beta} \langle X^{\alpha_1, \beta} \rangle - Z_{\beta, \alpha_1} \langle X^{\beta, \alpha_2} \rangle)}{\omega + E_{\bar{\alpha}} - i\frac{\gamma}{2}}. \quad (\text{A13})$$

Using (A7), and taking into account that the input is inserted through the left port ($l=1$) into the cavity, and the output is collected through the right one ($l=2$), we can write the transmission as

$$t_c(\omega) = \frac{\langle b_{out,2} \rangle}{\langle b_{in,1} \rangle} = \frac{i\sqrt{\kappa_1 \kappa_2}}{\Omega - \omega - i\frac{\kappa}{2} + g^2 \chi(\omega)} \quad (\text{A14})$$

which is the usual result for the cavity transmission, with $\chi(\omega)$ being the electronic susceptibility.

Using the mean-field Hamiltonian

If we instead consider the MF Hamiltonian for the cavity, topological system and their interaction, we start from the following expression

$$\begin{aligned} H &= \Omega d^{\dagger} d - \frac{g^2 \langle Z \rangle^2}{\Omega} + \tilde{H}_S + g (d^{\dagger} + d) \tilde{Z} \\ &\quad + \sum_{l=1,2} \int_{-\infty}^{\infty} \omega b_l^{\dagger}(\omega) b_l(\omega) d\omega \\ &\quad + i \sum_{l=1,2} \sqrt{\frac{\gamma_l}{2\pi}} \int_{-\infty}^{\infty} d\omega \left[b_l^{\dagger}(\omega) \left(d - \frac{g \langle Z \rangle}{\Omega} \right) \right. \\ &\quad \left. - \left(d^{\dagger} - \frac{g \langle Z \rangle}{\Omega} \right) b_l(\omega) \right] \end{aligned} \quad (\text{A15})$$

where $\tilde{Z} = Z - \langle Z \rangle$ and $\tilde{H}_S = H_S - \frac{2g^2\langle Z \rangle}{\Omega}Z$. Note that the cavity operators have been rotated to $\tilde{d}^{(\dagger)} = d^{(\dagger)} - \frac{g\langle Z \rangle}{\Omega}$ in order to diagonalize their MF Hamiltonian. The self-consistent values of $\langle Z \rangle$ and $\langle d^{(\dagger)} \rangle$ have been determined ignoring the coupling to the transmission line, as explained in the main text. Importantly, the cavity operators in H_B have also been rotated accordingly. This time, the EoM for $b_l(\nu, t)$ yields the following solution

$$\tilde{b}_l(\nu, t) = b_l(\nu, t) - \frac{g\langle Z \rangle}{\Omega} \sqrt{\frac{\kappa_l}{2\pi}} \frac{1 - e^{-i\nu(t-t_0)}}{i\nu} \quad (\text{A16})$$

Compared to (A4), we have an extra term due to the rotation of the bosonic operators, that depends on the state of the fermionic system through $\langle Z \rangle$. The EoM for $d(t)$ has the same form, with redefined input and output fields

$$\tilde{b}_{\text{in},l}(t) = b_{\text{in},l}(t) - \frac{g\sqrt{\kappa_l}\langle Z \rangle}{2\pi\Omega} \int_{-\infty}^{\infty} \frac{1 - e^{-i\nu(t-t_0)}}{i\nu} d\nu, \quad (\text{A17})$$

$$\tilde{b}_{\text{out},l}(t) = b_{\text{out},l}(t) + \frac{g\sqrt{\kappa_l}\langle Z \rangle}{2\pi\Omega} \int_{-\infty}^{\infty} \frac{1 - e^{i\nu(t_1-t)}}{i\nu} d\nu, \quad (\text{A18})$$

also fulfilling that $\tilde{b}_{\text{out},l}(t) = \tilde{b}_{\text{in},l}(t) + \sqrt{\kappa_l}d(t)$. On the other hand, the Hubbard operators change as well due to the presence of the extra MF contribution in the fermionic Hamiltonian

$$\tilde{H}_S = H_S - \frac{2g^2\langle Z \rangle}{\Omega}Z = \sum_{\alpha=1}^N \tilde{E}_\alpha \tilde{X}^{\alpha,\alpha}, \quad (\text{A19})$$

$$\tilde{Z} = \sum_{\tilde{\alpha}} \tilde{Z}_{\tilde{\alpha}} \tilde{X}^{\tilde{\alpha}}. \quad (\text{A20})$$

The EoM for \tilde{X} has the same form of (A9), but substituting the eigenvalues and eigenvectors of the unperturbed fermionic Hamiltonian H_S by the ones of MF Hamiltonian \tilde{H}_S . To solve the EoM, we take fluctuations to be small, which is a valid assumption when g is both small and very large, i.e., when the MF Hamiltonian $\tilde{H}_S + \tilde{H}_\Omega$ accurately describes the physics of the system, without considering the fluctuations Hamiltonian \tilde{H}_δ . Under this condition, we can write $d^{(\dagger)}(t) \tilde{X}(t) \approx \langle \tilde{X} \rangle d^{(\dagger)}(t) + \langle d^{(\dagger)} \rangle \tilde{X}(t)$. Again, we neglect any correlation created by the fluctuations Hamiltonian, which acts as an effective interaction between the two MF Hamiltonians. Note that $\langle d^{(\dagger)} \rangle = 0$ when evaluated using the MF photonic Hamiltonian in the rotated frame, \tilde{H}_Ω . Formally, the decoupling employed to solve (A20) is the

same as the one used in (A9). Then, the solution for \tilde{X} gives

$$\tilde{X}^{\tilde{\alpha}}(\omega) \simeq gd(\omega) \frac{\sum_{\beta} \left(\tilde{Z}_{\alpha_2,\beta} \langle \tilde{X}^{\alpha_1,\beta} \rangle - \tilde{Z}_{\beta,\alpha_1} \langle \tilde{X}^{\beta,\alpha_2} \rangle \right)}{\omega + \tilde{E}_{\tilde{\alpha}} - i\frac{\gamma}{2}}. \quad (\text{A21})$$

Note that (A13) is analogous to (A21), but all parameters have been renormalized due to MF. Finally, the transmission can be written as

$$t_c(\omega) = \frac{i\sqrt{\kappa_1\kappa_2}}{\Omega - \omega - i\frac{\kappa}{2} + g^2\tilde{\chi}(\omega)}. \quad (\text{A22})$$

where now $\tilde{\chi}(\omega)$ is the susceptibility written in terms of the MF Hamiltonian.

Appendix B: Transmission and photonic Green's function

The starting point is the EoM for the photonic operator $d(t)$ (A5) in Fourier space

$$\begin{aligned} i\omega d(\omega) &= -i\left(\Omega - i\frac{\kappa}{2}\right)d(\omega) - ig \sum_{\tilde{\alpha}} Z_{\tilde{\alpha}} \tilde{X}^{\tilde{\alpha}}(\omega) \\ &\quad - \sum_{l=1,2} \sqrt{\kappa_l} \tilde{b}_{\text{in},l}(\omega) \end{aligned} \quad (\text{B1})$$

The losses of the cavity have been included through the phenomenological factor κ . This equation depends on $\tilde{X}^{\tilde{\alpha}}(\omega)$, which has its own dynamics as well,

$$\begin{aligned} i\omega \tilde{X}^{ij}(\omega) &= -i\left(\tilde{E}_j - \tilde{E}_i + i\frac{\gamma}{2}\right) \tilde{X}^{ij}(\omega) \\ &\quad - ig\left(d^\dagger(\omega) + d(\omega)\right) \sum_m \left(Z_{jm} \tilde{X}^{im}(\omega) \right. \\ &\quad \left. - Z_{mi} \tilde{X}^{mj}(\omega) \right). \end{aligned} \quad (\text{B2})$$

Solving this equation implies writing the EoM for $d^{(\dagger)} \tilde{X}^{ij}$, which at the same time is coupled to higher-order operators. Then, we can write an infinite vector with all the relevant operators involved, $\vec{v} = (d, X^{ij}, \dots)$, and the system of equations turns out to be

$$(\omega - A) \vec{v} = \vec{v}_0 \quad (\text{B3})$$

where A is the coefficients matrix and \vec{v}_0 represents the inhomogeneous term.

Then, on the other hand, we can write the EoM for the retarded photonic Green function, defined as $G(t) = -i\theta(t)\langle [d(t), d^\dagger] \rangle \equiv \langle \langle d(t); d^\dagger \rangle \rangle_t$, yielding

$$\omega G(\omega) = 1 + \left(\Omega - i\frac{\kappa}{2}\right) \tilde{G}(\omega) + g \sum_{ij} M_{ij}(\omega) \quad (\text{B4})$$

where $\tilde{M}_{ij}(\omega) = \langle \langle X^{ij}; a^\dagger \rangle \rangle_\omega$. Note that the dissipative factor enters the EoM for $G(\omega)$ through the integration of the external modes and their coupling to the cavity photons, just as in Eq. A5. Again, this EoM is coupled to higher-order Green functions, resulting in an infinite system of coupled differential equations. In matrix form, we have

$$(\omega - A') \vec{V}(\omega) = \vec{V}_0 \quad (\text{B5})$$

where $\vec{V} = (G, M_{ij}, \dots)$ and \vec{V}_0 is the inhomogeneous term by comparison. One can see that $A = A'$, which indicates that $G(\omega) = -i\theta(t)\langle [a(t), a^\dagger] \rangle$ is the resolvent of (B1).

Finally, we can compare the first component of each system of equations, namely $a(\omega) = -i(\omega - H)^{-1} \sum_{l=1,2} \sqrt{\kappa_l} \tilde{b}_{\text{in},l}(\omega)$ and $G(\omega) = (\omega - H)^{-1}$, and see that

$$a(\omega) = -iG(\omega) \sum_{l=1,2} \sqrt{\kappa_l} \tilde{b}_{\text{in},l}(\omega). \quad (\text{B6})$$

The last step is to write the transmission as a function of $a(\omega)$, knowing that $\tilde{b}_{\text{out},l}(t) = \tilde{b}_{\text{in},l}(\omega) + \sqrt{\kappa_l} a(\omega)$ and that the only input is through port 1

$$t_c = \frac{\langle \tilde{b}_{\text{out},2} \rangle}{\langle \tilde{b}_{\text{in},1} \rangle} = \frac{\langle \tilde{b}_{\text{in},2} \rangle + \sqrt{\kappa_2} \langle a \rangle}{\langle \tilde{b}_{\text{in},1} \rangle} = -i\sqrt{\kappa_2} \sqrt{\kappa_1} G(\omega). \quad (\text{B7})$$

It is very enlightening to obtain an analytical expression for the photonic Green function in the case of $g \ll \Omega, \tilde{E}_{\tilde{\alpha}}$ and $g \gg \Omega, \tilde{E}_{\tilde{\alpha}}$. The equation of motion of $G(\omega)$ (Eq. B4) is coupled to the mixed Green function \tilde{M}_{ij} , which gives

$$\begin{aligned} \omega \tilde{M}_{ij} &= (\tilde{E}_j - \tilde{E}_i) \tilde{M}_{ij} + \sum_l Z_{jl} \langle \langle (d^\dagger + d) \tilde{X}^{il}; d^\dagger \rangle \rangle_\omega \\ &\quad - \sum_l Z_{li} \langle \langle (d^\dagger + d) \tilde{X}^{lj}; d^\dagger \rangle \rangle \end{aligned} \quad (\text{B8})$$

Note the presence of the higher-order Green function $\langle \langle (d^\dagger + d) \tilde{X}; d^\dagger \rangle \rangle$. Fluctuations are negligible in the

regimes considered, which let us employ the following decoupling scheme

$$\begin{aligned} \langle \langle (d^\dagger + d) \tilde{X}; d^\dagger \rangle \rangle &\approx (\langle d^\dagger \rangle + \langle d \rangle) \langle \langle \tilde{X}; d^\dagger \rangle \rangle_\omega \\ &\quad + \langle \tilde{X} \rangle \langle \langle d; d^\dagger \rangle \rangle_\omega \end{aligned} \quad (\text{B9})$$

This approximation is analogous to the one presented in Eq. 11 in the main text. Again, it implies that we are neglecting first-order correlations between fermionic and photonic operators, and under this assumption the system of equations including Eqs. B4 and B8 can be closed and solved, obtaining

$$G(\omega) = -\frac{1}{\Omega - \omega + g^2 \tilde{\chi}(\omega)}. \quad (\text{B10})$$

for the photonic Green function. It is straight-forward to see that the previous expression verifies the relation between the transmission and $G(\omega)$ presented in Eq. 9, when compared with Eq. 12 in the limits of $g \ll \Omega, \tilde{E}_{\tilde{\alpha}}$ and $g \gg \Omega, \tilde{E}_{\tilde{\alpha}}$.

Appendix C: Solution for $\langle Z \rangle$

In order to solve the self-consistency equation for the order parameter $\langle Z \rangle = \sum_{\tilde{\alpha}} \tilde{Z}_{\tilde{\alpha}} \langle \tilde{X}^{\tilde{\alpha}} \rangle$, we iterate until convergence using the eigenstates of the MF Hamiltonian \tilde{H}_S in Eq. 4, and also those of the total Hamiltonian $\tilde{H}_\delta + \tilde{H}_S + \tilde{H}_\Omega$ to compare with the exact value.

Fig. 6 shows $\langle Z \rangle$ as a function of g for the MF case and the exact one, and provides us a precise value for the breakdown of the approximation. Different chain lengths N have also been considered. As expected, the MF calculation agrees with the exact value at small and large g . In the former case, $\langle Z \rangle = 0$ indicates that the MF Hamiltonian coincides with the free Hamiltonian, and that the symmetries of the model are unaffected by the coupling with the cavity. In the latter, the system polarizes (i.e., $\langle Z \rangle \neq 0$) indicating that the ground state of the system is modified and that certain symmetries change. For intermediate values, fluctuations take over and lead to disagreement between the MF and the exact solution. The MF result indicates that the change in $\langle Z \rangle$ is continuous, corresponding to a second-order phase transition. However, the exact calculation shows a discontinuity at a critical value for g , which could indicate that is in fact a first order transition.

Interestingly, we find that beyond the critical g a difference between the topological and the trivial phase arises, which is also captured by the MF solution. This is a

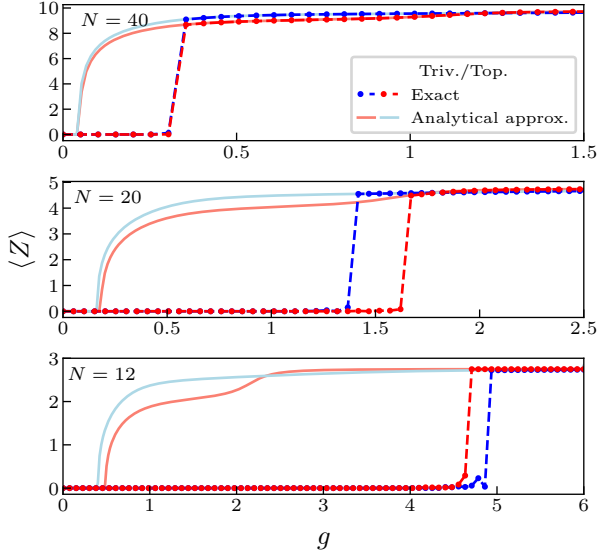


Figure 6: $\langle Z \rangle$ for different N . $\langle Z \rangle$ as a function of the coupling constant g for $\Omega = 10$, $\delta = \pm 0.6$ (trivial/topological phase) and different system sizes: $N = 40$ (top), $N = 20$ (middle), $N = 12$ (bottom). The value of $\langle Z \rangle$ has been calculated self-consistently using the MF Hamiltonian (solid) and exact diagonalization (dashes and dots). The chain size modifies the value of the critical point at which the system polarizes, enhancing or reducing the difference between topological phases at the phase transition

consequence of the different coupling between bulk/edge modes and the cavity photons. It also indicates that certain features of the topological edge states still remain when the coupling strength is increased beyond the small g regime, but they disappear again at very large g .

$\langle Z \rangle$ also depends on the chain length N . This is intuitive due to the position-dependent interaction: the chain size modifies the value of the critical point at which the system polarizes, enhancing or reducing the difference between topological phases at the phase transition, as well as the final value in the limit $g \rightarrow \infty$. Also, as the number of sites N increases, the critical value of g at which the phase transition happens is reduced (see Fig. 6). This is expected, since the effective strength of the coupling at each site $g_i = gx_i$ gets larger as more sites are considered.

The system size also shapes the differences between topological phases found immediately after the phase transition, that are captured by the MF calculation, without including fluctuations.

Appendix D: Schrieffer-Wolff transformation

We begin with the Hamiltonian $H = \tilde{H}_S + \tilde{H}_\Omega + \tilde{H}_\delta$, as defined in the main text, written in the basis of eigenstates of \tilde{H}_S :

$$H = \sum_i \tilde{E}_\alpha \tilde{X}^{\alpha,\alpha} + \Omega d^\dagger d - \frac{g^2 \langle Z \rangle}{\Omega} + g(d^\dagger + d)\tilde{Z} \quad (\text{D1})$$

We propose the following ansatz for the generator S of the Schrieffer-Wolff (S-W) transformation,

$$S = \sum_{\vec{\alpha}} (\Gamma_{\vec{\alpha}}^+ d^\dagger + \Gamma_{\vec{\alpha}}^- d) \tilde{X}^{\vec{\alpha}} \quad (\text{D2})$$

where $\vec{\alpha} = (\alpha_1, \alpha_2)$. Imposing $\tilde{H}_\delta = -[S, \tilde{H}_S + \tilde{H}_\Omega]$, one finds the following equations for the free parameters:

$$\Gamma_{\vec{\alpha}}^\pm = \frac{g \tilde{Z}_{\vec{\alpha}}}{\tilde{E}_{\vec{\alpha}} \pm \Omega}. \quad (\text{D3})$$

with $\tilde{E}_{\vec{\alpha}} = \tilde{E}_{\alpha_1} - \tilde{E}_{\alpha_2}$. This results in the final form of the transformation:

$$S = g(d^\dagger + d) \sum_{\vec{\alpha}} \frac{\tilde{E}_{\vec{\alpha}} \tilde{Z}_{\vec{\alpha}}}{\tilde{E}_{\vec{\alpha}}^2 - \Omega^2} - g\Omega(d^\dagger - d) \sum_{ij} \frac{\tilde{Z}_{\vec{\alpha}}}{\tilde{E}_{\vec{\alpha}}^2 - \Omega^2} \tilde{X}^{\vec{\alpha}} \quad (\text{D4})$$

The correction to the Hamiltonian is proportional to:

$$\begin{aligned} [S, \tilde{H}_\delta] &= g^2(d^\dagger + d)^2 \sum_{\vec{\alpha}} \frac{\tilde{E}_{\vec{\alpha}} \tilde{Z}_{\vec{\alpha}}}{\tilde{E}_{\vec{\alpha}}^2 - \Omega^2} Y_{\vec{\alpha}}^- \\ &\quad - g^2 \Omega (d^{\dagger 2} - d^2) \sum_{\vec{\alpha}} \frac{\tilde{Z}_{\vec{\alpha}}}{\tilde{E}_{\vec{\alpha}}^2 - \Omega^2} Y_{\vec{\alpha}}^- \\ &\quad + g^2 \Omega \sum_{\vec{\alpha}} \frac{\tilde{Z}_{\vec{\alpha}}}{\tilde{E}_{\vec{\alpha}}^2 - \Omega^2} Y_{\vec{\alpha}}^+ \end{aligned} \quad (\text{D5})$$

with

$$Y_{\vec{\alpha}}^\pm = \sum_{\beta} (\tilde{Z}_{\alpha_2 \beta} \tilde{X}^{\alpha_1 \beta} \pm \tilde{Z}_{\beta \alpha_1} X^{\beta \alpha_2}) \quad (\text{D6})$$

Finally, one can write the effective Hamiltonian up to second order, neglecting two-photon processes and constant terms,

$$\begin{aligned} \bar{H} &\simeq \tilde{H}_S + \Omega d^\dagger d + \frac{1}{2} [S, \tilde{H}_\delta] \\ &= \sum_{\alpha} \tilde{E}_{\alpha} \tilde{X}^{\alpha,\alpha} \\ &\quad + \frac{g^2}{2} \sum_{\vec{\alpha}} \tilde{Z}_{\vec{\alpha}} \left[\frac{\sum_{\beta} \tilde{Z}_{\alpha_2 \beta} \tilde{X}^{\alpha_1 \beta}}{\tilde{E}_{\vec{\alpha}} - \Omega} - \frac{\sum_n \tilde{Z}_{\beta \alpha_1} \tilde{X}^{\beta \alpha_2}}{\tilde{E}_{\vec{\alpha}} + \Omega} \right] \\ &\quad + \left[\Omega + g^2 \sum_{\vec{\alpha}} \tilde{\Omega}_{\vec{\alpha}} \tilde{Y}_{\vec{\alpha}}^- \right] d^\dagger d. \end{aligned} \quad (\text{D7})$$

where $\tilde{\Omega}_\alpha$ is defined in the main text.

Appendix E: Entanglement Entropy and Energy Spectrum

As shown in Fig. 6(c) in the main text, there is a $\log(2)$ -plateau in the topological phase for small- g when the $N/2$ -th state is occupied, corresponding to one of the topological edge states. Its drop at $g \sim 0.84$ corresponds with its anti-crossing with a state belonging to the bulk bands and indicates the destruction of maximal entanglement for the $N/2$ -th state.

However, the topological contribution to the entanglement entropy is not lost at this point, but migrates from one state to the other as they further anti-cross in the energy spectrum. Figure 7 shows a zoom of the energy

spectrum where the edge states penetrate into the bulk bands, together with the entanglement entropy S_A associated to the occupation of each of them. For small- g , the $\log(2)$ plateau corresponds to the $N/2$ -th (red) and $(N/2 + 1)$ -th (yellow) states (edge states), while the rest of them are not maximally entangled (their S_A depends on the partition used). The first anti-crossing encountered in the spectrum (at $g \sim 0.78$) between the yellow and blue (top state in the valence band) states, corresponds to the appearance of a $\log(2)$ -plateau for the later, while the entanglement between the ending sites is lost for the edge state.

On the other hand, as g is increased, the $N/2$ -th state anti-crosses with other states as well. Figure 8 shows that each of these anti-crossings correspond to the abrupt changes in S_A obtained for the $N/2$ -th state (Fig. 6C), by zooming into the first four of them.

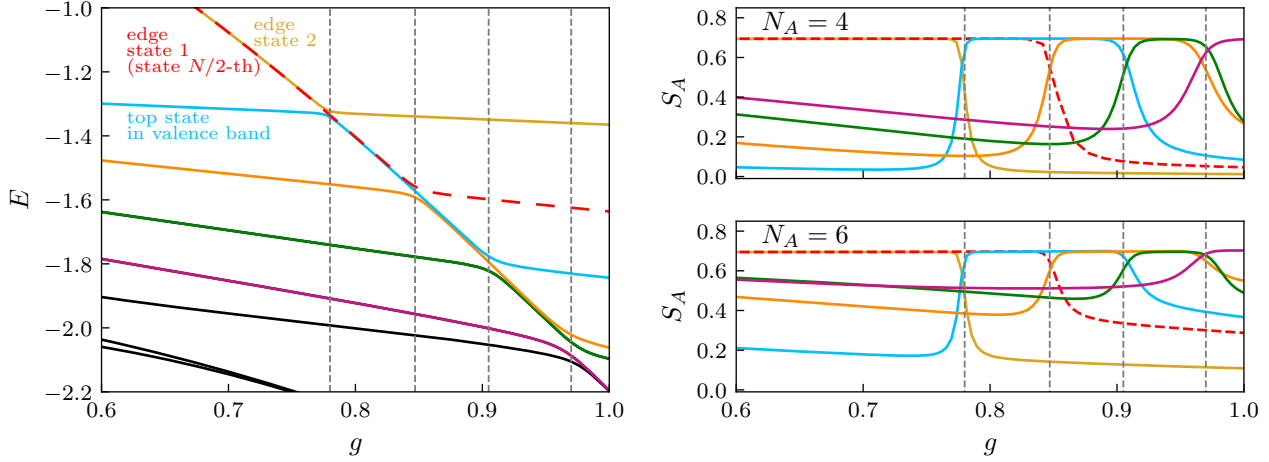


Figure 7: **Entanglement entropy and the energy spectrum.** Left plot: zoom into the energy spectrum, as a function of g , corresponding to the anti-crossing (dashed, grey vertical lines) of energy states triggered by the entrance of the edge states into the bulk band. The parameters chosen are: $\Omega = 10$ $\delta = -0.6$, $N = 20$. Each state is depicted in a different color: yellow for the $(\frac{N}{2} + 1)$ -th state, red for the $N/2$ -th (corresponding to the two edge states), blue for the $(\frac{N}{2} - 1)$ -th (top state in the valence band), orange for the $(\frac{N}{2} - 2)$ -th, green for the $(\frac{N}{2} - 3)$ -th and violet for the $(\frac{N}{2} - 4)$ -th (the following states appear in black). The first anti-crossing at $g \sim 0.78$ happens between the edge state (yellow) and the top state in the valence band (blue). The second anti-crossing at $g \sim 0.9$ happens between the edge state (red) and $(\frac{N}{2} - 2)$ -th state in the bulk band (orange). For higher values of the coupling constant (only shown up to $g = 1$), successive anti-crossings between adjacent states appear. Right plot: entanglement entropy for each state (same color code as in the left plot), for different partitions $N = 4$ (upper plot) and $N = 6$ (lower plot). For small- g , the $\log(2)$ plateau corresponds to the $N/2$ -th state, while the rest of them are not maximally entangled (their S_A depends on the partition used). Each time a state from the bulk band anti-crosses with an edge state, it turns into an edge state itself, so that the $\log(2)$ plateau (originally caused by the non-trivial topology of the fermionic system) migrates from one state to the other.

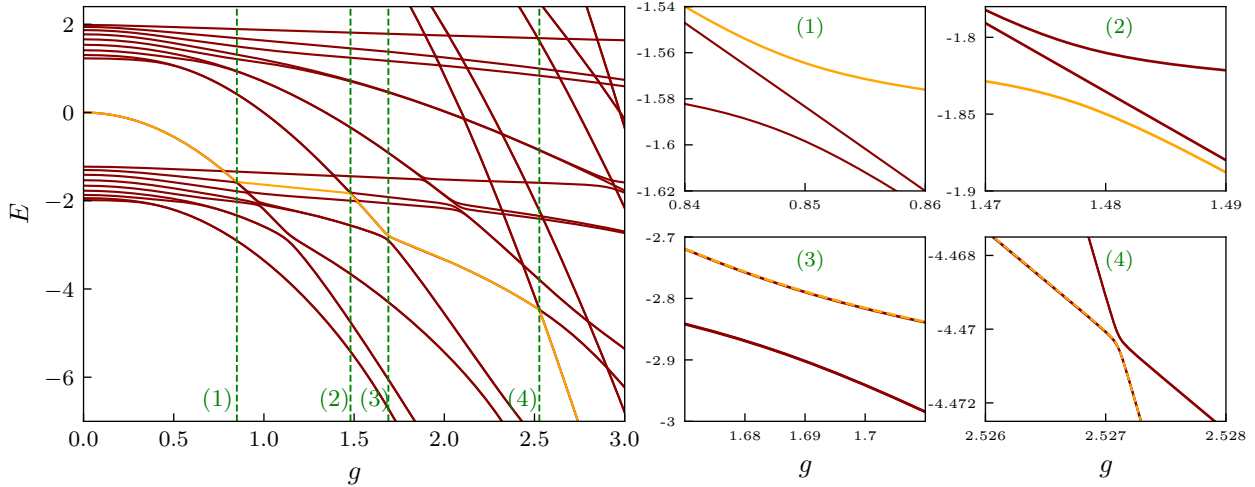


Figure 8: **Anti-crossings for the $N/2^{\text{th}}$ state in the topological phase.** Left plot: energy spectrum for the zero-photon band as a function of g . The $N/2$ -th state (for which the entanglement entropy is calculated in Fig. 6(c)) is represented in orange. The green, dashed lines represent the first four anti-crossings for this state, which correspond to the first four abrupt changes in S_A in Fig. 6(c). Right plots: zoom into the first four anti-crossings of the $N/2$ -th state.